ARG   H&E $\alpha_v\beta_3$ integrin

A

B

FIGURE 4. Ex vivo autoradiography [A,[18]F-FDG; B, ^{111}In-DOTA-c(RGDfK)] and histopathologic analysis of inflammation induced by turpentine oil in mouse model. Sections of inflammatory regions were stained with hematoxylin–eosin (H&E) and anti–$\alpha_v\beta_3$-integrin antibody.

model (Fig. 4 and Fig. 5). In this model, acute inflammation was characterized by focal neutrophil infiltration (Fig. 4). Although ^{18}F-FDG was actively taken up in the inflammatory regions in all cases, ^{111}In-DOTA-c(RGDfK) was not. There was no expression of $\alpha_v\beta_3$-integrin in this inflammatory model. The inflammation-to-muscle ratio for ^{18}F-FDG was much higher than that for ^{111}In-DOTA-c(RGDfK) (8.37 ± 4.37 vs. 1.98 ± 0.60; $P < 0.05$) (Fig. 5).

DISCUSSION

Because $\alpha_v\beta_3$-integrin is often expressed in various kinds of malignant tumors and endothelial cells, tumor imaging with radiolabeled RGD peptides, which are promising agents for $\alpha_v\beta_3$-integrin imaging, has been actively investigated in animal models and cancer patients (26–29). Haubner et al. showed that there was a correlation between the tumor uptake of ^{18}F-galacto-c(RGDfK) and the level of $\alpha_v\beta_3$-integrin expression (27). We developed ^{111}In-DOTA-c(RGDfK), an ^{111}In-labeled RGD, and demonstrated that this radiopharmaceutical showed high tumor uptake in SKOV-3, a human ovarian carcinoma model, with strong expression of $\alpha_v\beta_3$-integrin (29).

Pancreatic cancer, one of the most incurable malignant tumors, can also be imaged with radiolabeled RGD peptides because pancreatic cancer cells express $\alpha_v\beta_3$-integrin (18). However, successful cure of pancreatic cancer requires detection in the early stages of carcinogenesis, when the lesions are small. For this purpose, suitable animal models that mimic the clinical situation as closely as possible are ideal tools. The hamster model used in the present study is well established and has been used for numerous studies of pancreatic duct carcinogenesis and its prevention (20,32,33). Because this carcinogenesis model appeared to be suitable for evaluation of the usefulness of imaging agents in the early detection of pancreatic cancer, we investigated the possibility of early and accurate detection of this cancer by combining this model and SPECT with ^{111}In-DOTA-c(RGDfK).

In the present study, SPECT with ^{111}In-DOTA-c(RGDfK) clearly demonstrated 66.7% of pancreatic adenocarcinomas in the hamster model. The smallest pancreatic adenocarcinoma detected was 3 mm. This encouraging finding regarding the detection of early pancreatic cancer was validated by the high T/N ratio, as shown by ARG. This good contrast between tumors and normal tissues may be explained by the fact that $\alpha_v\beta_3$-integrin is strongly expressed in adenocarcinoma lesions but not in stroma and normal ductal cells. Our histopathologic examination reconfirmed this finding. The results of the present study demonstrated that our strategy of using $\alpha_v\beta_3$-integrin as a molecular target was entirely appropriate. Especially important was the fact that SPECT yielded no false-positive findings in normal pancreatic tissue.
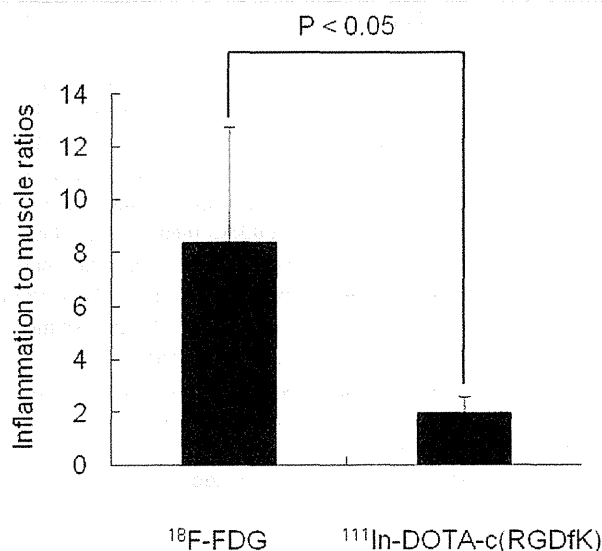

FIGURE 5. Ratios of inflammation to muscle for ^{18}F-FDG and ^{111}In-DOTA-c(RGDfK), as calculated by ARG analysis ($n = 4$).

ARG analysis demonstrated positive uptake in atypical hyperplasia, but SPECT did not. One reason for this difference could be lesion size. The average size of atypical hyperplasia lesions is 1.0 mm—too small for detection by in vivo SPECT. Another reason could be that the uptake of ^{111}In-DOTA-c (RGDfK) in atypical hyperplasia was relatively lower than that in adenocarcinomas; however, this reason suggests that $\alpha_v\beta_3$-integrin would be a good target for the early detection of pancreatic cancer with radiolabeled RGD peptides because atypical hyperplasia lesions can be regarded as precancerous lesions in terms of carcinogenesis.

In the clinical application of SPECT with ^{111}In-DOTA-c(RGDfK), it is important to clarify the anatomic location of the radionuclide uptake. In the present study, we used a SPECT/CT combination scanner, although this scanner was dedicated to small-animal imaging. Through SPECT/CT fusion imaging, we identified the pancreas on the basis of the location of the kidneys, liver, intestine, and stomach, which are relatively clearly visualized on CT. SPECT/CT combination scanners are becoming popular in clinical practice. Because the performance of clinical CT scanners is better than that of small-animal units with regard to acquisition time, tube voltage, and current × time product (mAs), identification of the pancreas would be easier in clinical practice. Fusion imaging with MRI and scintigraphy is now actively under investigation. Current high-magnetic-field MRI scanners can provide high-resolution anatomic images without contrast agents. Therefore, fusion imaging with MRI and PET or SPECT would overcome the concern about identification of the pancreas (34).

^{18}F-FDG PET may have become more popular for the detection of malignant tumors, but ^{18}F-FDG also has a high affinity for inflammatory lesions, resulting in false-positive findings. Because pancreatic masses or swellings are sometimes caused by inflammatory changes, ^{18}F-FDG PET may produce false-positive results. To examine whether SPECT with ^{111}In-DOTA-c(RGDfK) is more useful than ^{18}F-FDG PET in the differentiation of inflammatory lesions, we compared the uptake of ^{111}In-DOTA-c(RGDfK) in inflammatory lesions induced by turpentine in a mouse inflammatory model with the uptake of ^{18}F-FDG. The uptake of ^{111}In-DOTA-c(RGDfK) in inflammatory lesions and the expression of $\alpha_v\beta_3$-integrin were not found, resulting in a significantly lower inflammation-to-muscle ratio for ^{111}In-DOTA-c(RGDfK) than for ^{18}F-FDG. In contrast, ARG indicated high ^{18}F-FDG uptake in inflammatory lesions, in agreement with a previous report (31). This profile of $\alpha_v\beta_3$-integrin expression is favorable for distinguishing between tumors and inflammation. In pancreatic lesions, false-positive results for the detection of cancer may be harmful because pancreatic biopsy is somewhat invasive. Therefore, ^{111}In-DOTA-c(RGDfK) may be superior to ^{18}F-FDG for the early and accurate detection of pancreatic cancer.

CONCLUSION

The results of the present study indicated that SPECT with ^{111}In-DOTA-c(RGDfK) is a powerful tool for the di-

agnosis of pancreatic cancer in the hamster carcinogenesis model, even though a limitation was imposed by the small number of animals evaluated. The specific uptake of ^{111}In-DOTA-c(RGDfK) in tumors and not in inflammatory lesions could decrease the incidence of false-positive findings. Our results will promote the clinical application of ^{111}In-DOTA-c(RGDfK) and other $\alpha_v\beta_3$-integrin imaging agents in the diagnosis of pancreatic cancer.

REFERENCES

1. Qiu D, Katanoda K, Marugame T, Sobue T. A Joinpoint regression analysis of long-term trends in cancer mortality in Japan (1958-2004). *Int J Cancer.* 2009;124:443–448.
2. Jemal A, Siegel R, Xu J, Ward E. Cancer statistics, 2010. *CA Cancer J Clin.* 2010;60:277–300.
3. Tsukuma H, Ajiki W, Ioka A, Oshima A. Survival of cancer patients diagnosed between 1993 and 1996: a collaborative study of population-based cancer registries in Japan. *Jpn J Clin Oncol.* 2006;36:602–607.
4. Li D, Xie K, Wolff R, Abbruzzese JL. Pancreatic cancer. *Lancet.* 2004;363:1049–1057.
5. Pongprasobchai S, Pannala R, Smyrk TC, et al. Long-term survival and prognostic indicators in small (≤2 cm) pancreatic cancer. *Pancreatology.* 2008;8:587–592.
6. Agarwal B, Correa AM, Ho L. Survival in pancreatic carcinoma based on tumor size. *Pancreas.* 2008;36:e15–e20.
7. Kauhanen SP, Komar G, Seppanen MP, et al. A prospective diagnostic accuracy study of ^{18}F-fluorodeoxyglucose positron emission tomography/computed tomography, multidetector row computed tomography, and magnetic resonance imaging in primary diagnosis and staging of pancreatic cancer. *Ann Surg.* 2009;250:957–963.
8. Sendler A, Avril N, Helmberger H, et al. Preoperative evaluation of pancreatic masses with positron emission tomography using ^{18}F-fluorodeoxyglucose: diagnostic limitations. *World J Surg.* 2000;24:1121–1129.
9. Okano K, Kakinoki K, Akamoto S, et al. ^{18}F-fluorodeoxyglucose positron emission tomography in the diagnosis of small pancreatic cancer. *World J Gastroenterol.* 2011;17:231–235.
10. Delbeke D, Pinson CW. Pancreatic tumors: role of imaging in the diagnosis, staging, and treatment. *J Hepatobiliary Pancreat Surg.* 2004;11:4–10.
11. Diederichs CG, Staib L, Vogel J, et al. Values and limitations of ^{18}F-fluorodeoxyglucose-positron-emission tomography with preoperative evaluation of patients with pancreatic masses. *Pancreas.* 2000;20:109–116.
12. Shreve PD. Focal fluorine-18 fluorodeoxyglucose accumulation in inflammatory pancreatic disease. *Eur J Nucl Med.* 1998;25:259–264.
13. Delbeke D, Rose DM, Chapman WC, et al. Optimal interpretation of FDG PET in the diagnosis, staging, and management of pancreatic carcinoma. *J Nucl Med.* 1999;40:1784–1791.
14. Diederichs CG, Staib L, Glatting G, Beger HG, Reske SN. FDG PET: elevated plasma glucose reduces both uptake and detection rate of pancreatic malignancies. *J Nucl Med.* 1998;39:1030–1033.
15. Brooks PC. Role of integrins in angiogenesis. *Eur J Cancer.* 1996;32A:2423–2429.
16. Brooks PC, Clark RA, Cheresh DA. Requirement of vascular integrin $\alpha_v\beta_3$ for angiogenesis. *Science.* 1994;264:569–571.
17. Mizejewski GJ. Role of integrins in cancer: survey of expression patterns. *Proc Soc Exp Biol Med.* 1999;222:124–138.

18. Hosotani R, Kawaguchi M, Masui T, et al. Expression of integrin $\alpha_v\beta_3$ in pancreatic carcinoma: relation to MMP-2 activation and lymph node metastasis. *Pancreas.* 2002;25:e30–e35.
19. Mizumoto K, Tsutsumi M, Denda A, Konishi Y. Rapid production of pancreatic carcinoma by initiation with *N*-nitroso-bis(2-oxopropyl)amine and repeated augmentation pressure in hamsters. *J Natl Cancer Inst.* 1988;80:1564–1567.
20. Takahashi M, Kitahashi T, Ishigamori R, et al. Increased expression of inducible nitric oxide synthase (iNOS) in *N*-nitrosobis(2-oxopropyl)amine-induced hamster pancreatic carcinogenesis and prevention of cancer development by ONO-1714, an iNOS inhibitor. *Carcinogenesis.* 2008;29:1608–1613.
21. Nishikawa A, Furukawa F, Imazawa T, Yoshimura H, Mitsumori K, Takahashi M. Effects of caffeine, nicotine, ethanol and sodium selenite on pancreatic carcinogenesis in hamsters after initiation with *N*-nitrosobis(2-oxopropyl)amine. *Carcinogenesis.* 1992;13:1379–1382.
22. Pour P, Althoff J, Kruger FW, Mohr U. A potent pancreatic carcinogen in Syrian hamsters: *N*-nitrosobis(2-oxopropyl)amine. *J Natl Cancer Inst.* 1977;58:1449–1453.
23. Fujii H, Egami H, Chaney W, Pour P, Pelling J. Pancreatic ductal adenocarcinomas induced in Syrian hamsters by *N*-nitrosobis(2-oxopropyl)amine contain a c-Ki-ras oncogene with a point-mutated codon 12. *Mol Carcinog.* 1990;3:296–301.
24. Tsutsumi M, Kondoh S, Noguchi O, et al. K-ras gene mutation in early ductal lesions induced in a rapid production model for pancreatic carcinomas in Syrian hamsters. *Jpn J Cancer Res.* 1993;84:1101–1105.
25. Kitahashi T, Yoshimoto M, Imai T. Novel immunohistochemical marker, integrin $\alpha_v\beta_3$, for BOP-induced early lesions in hamster pancreatic ductal carcinogenesis. *Oncol Lett.* 2011;2:229–234.
26. Beer AJ, Schwaiger M. Imaging of integrin $\alpha_v\beta_3$ expression. *Cancer Metastasis Rev.* 2008;27:631–644.
27. Haubner R, Weber WA, Beer AJ, et al. Noninvasive visualization of the activated $\alpha_v\beta_3$ integrin in cancer patients by positron emission tomography and [18F]galacto-RGD. *PLoS Med.* 2005;2:e70.
28. Haubner R, Wester HJ, Weber WA, et al. Noninvasive imaging of $\alpha_v\beta_3$ integrin expression using 18F-labeled RGD-containing glycopeptide and positron emission tomography. *Cancer Res.* 2001;61:1781–1785.
29. Yoshimoto M, Ogawa K, Washiyama K, et al. $\alpha_v\beta_3$ Integrin-targeting radionuclide therapy and imaging with monomeric RGD peptide. *Int J Cancer.* 2008; 123:709–715.
30. Liu RS, Chou TK, Chang CH, et al. Biodistribution, pharmacokinetics and PET imaging of [18F]FMISO, [18F]FDG and [18F]FAc in a sarcoma- and inflammation-bearing mouse model. *Nucl Med Biol.* 2009;36:305–312.
31. Yamada S, Kubota K, Kubota R, Ido T, Tamahashi N. High accumulation of fluorine-18-fluorodeoxyglucose in turpentine-induced inflammatory tissue. *J Nucl Med.* 1995;36:1301–1306.
32. Nishikawa A, Furukawa F, Lee IS, Tanaka T, Hirose M. Potent chemopreventive agents against pancreatic cancer. *Curr Cancer Drug Targets.* 2004;4:373–384.
33. Takeuchi Y, Takahashi M, Sakano K, et al. Suppression of *N*-nitrosobis(2-oxopropyl) amine-induced pancreatic carcinogenesis in hamsters by pioglitazone, a ligand of peroxisome proliferator-activated receptor gamma. *Carcinogenesis.* 2007;28:1692–1696.
34. Tatsumi M, Isohashi K, Onishi H, et al. 18F-FDG PET/MRI fusion in characterizing pancreatic tumors: comparison to PET/CT. *Int J Clin Oncol.* 2011;16:408–415.

Research Article

In Vivo Visualization of Heterogeneous Intratumoral Distribution of Hypoxia-Inducible Factor-1α Activity by the Fusion of High-Resolution SPECT and Morphological Imaging Tests

Hirofumi Fujii,[1] Masayuki Yamaguchi,[1] Kazumasa Inoue,[1] Yasuko Mutou,[1] Masashi Ueda,[2] Hideo Saji,[2] Shinae Kizaka-Kondoh,[3] Noriyuki Moriyama,[4] and Izumi O. Umeda[1]

[1] *Functional Imaging Division, National Cancer Center Hospital East, Kashiwa 277-8577, Japan*
[2] *Graduate School of Pharmaceutical Sciences, Kyoto University, Kyoto 606-8501, Japan*
[3] *Graduate School of Bioscience and Biotechnology, Tokyo Institute of Technology, Yokohama 226-8503, Japan*
[4] *Research Center for Cancer Prevention and Screening, National Cancer Center, Tokyo 104-0045, Japan*

Correspondence should be addressed to Izumi O. Umeda, ioumeda@east.ncc.go.jp

Purpose. We aimed to clearly visualize heterogeneous distribution of hypoxia-inducible factor 1α (HIF) activity in tumor tissues *in vivo.* *Methods.* We synthesized of ^{125}I-IPOS, a ^{125}I labeled chimeric protein probe, that would visualize HIF activity. The biodistribution of ^{125}I-IPOS in FM3A tumor-bearing mice was evaluated. Then, the intratumoral localization of this probe was observed by autoradiography, and it was compared with histopathological findings. The distribution of ^{125}I-IPOS in tumors was imaged by a small animal SPECT/CT scanner. The obtained *in vivo* SPECT-CT fusion images were compared with *ex vivo* images of excised tumors. Fusion imaging with MRI was also examined. *Results.* ^{125}I-IPOS well accumulated in FM3A tumors. The intratumoral distribution of ^{125}I-IPOS by autoradiography was quite heterogeneous, and it partially overlapped with that of pimonidazole. High-resolution SPECT-CT fusion images successfully demonstrated the heterogeneity of ^{125}I-IPOS distribution inside tumors. SPECT-MRI fusion images could give more detailed information about the intratumoral distribution of ^{125}I-IPOS. *Conclusion.* High-resolution SPECT images successfully demonstrated heterogeneous intratumoral distribution of ^{125}I-IPOS. SPECT-CT fusion images, more favorably SPECT-MRI fusion images, would be useful to understand the features of heterogeneous intratumoral expression of HIF activity *in vivo.*

1. Introduction

It is very important for the optimization of treatments of tumors to evaluate their features. The features of tumors are usually investigated by pathological examination using some pieces of biopsied specimens. But the pathological findings inside the tumor are often heterogeneous. For example, the expression of human epidermal growth factor receptor 2 (HER2) is often heterogeneous in breast cancer tissues [1]. This means that the degree of HER2 expression can be differently diagnosed according to the biopsy site even in the same tumor. Since, the indication of trastuzumab therapy for

breast cancer is determined on the basis of the expression of HER2, the indication of this therapy might also be judged differently according to the biopsy site. To resolve this issue, imaging tests would be useful because they can observe the whole of tumors, unlike pathological tests using biopsied specimens.

There are many studies to evaluate the features of tumors using imaging tests. For example, ^{18}F-fluorodeoxyglucose (FDG) positron emission tomography (PET) has been used to observe glucose metabolism in tumors [2]. And this imaging test is now routinely performed in the clinical practice. Although these imaging tests could image the whole

of tumors, they usually failed to visualize the heterogeneity of tumors due to their poor spatial resolution.

But recent advances in imaging devices and image processing methods have enabled to provide excellent images with high spatial resolution. And it has been also reported that the superimposition of images showing functional information on morphological images such as CT and MRI is quite useful to understand the features of tumors [3]. We will be able to investigate heterogeneous features inside tumors more precisely by using these techniques, and the obtained results will contribute to the optimization of cancer therapy.

Tumor hypoxia is one of the main reasons for the resistance to anticancer therapy such as radiotherapy and chemotherapy [4, 5]. The oxygen partial pressure is heterogeneously distributed in tissues since it depends on intratumoral vasculature [6]. It is difficult to diagnose this heterogeneity in oxygen partial pressure in cancer tissues by biopsied specimens. In some studies, oxygen partial pressure in tumors was measured by inserting an oxygen electrode [7]. But this method is rather invasive and not easy to repeat due to patients' pain. It is also difficult to investigate its heterogeneous distribution in the tumor. Therefore, it is expected to visualize the heterogeneous intratumoral distribution of oxygen partial pressure by *in vivo* imaging tests with high spatial resolution.

Although immunohistological staining by pimonidazole is often used in experimental studies, its clinical application is impossible because pimonidazole cannot be injected into humans due to its toxicity.

Overexpression of hypoxia inducible factor (HIF) partially contributes to the resistance to antitumor therapies under hypoxic conditions [8]. We are interested in evaluating HIF activity as a surrogate of direct measuring of oxygen partial pressure. Recently, an idea where HIF activity is evaluated utilizing the stability of oxygen-dependent degradation (ODD) domain in HIF was reported in the field of optical imaging. And HIF activity was successfully visualized using an optical probe obtained by the fusion of ODD and protein transduction domain (PTD) [9, 10]. As the clinical application of optical imaging techniques is quite limited, its translation in the field of nuclear medicine is expected.

Kudo et al. imaged HIF-1-active tumor hypoxia using a similar chimeric protein probe, ^{123}I-IPOS, a conjugate of ^{123}I-labeled 3-iodobenzoyl norbiotinamide (IBB) and a fusion protein consisting of PTD, ODD, and streptavidin (POS) using a planar gamma camera [11, 12]. Although they could image the tumor itself as a mass, it was difficult to visualize the intratumoral heterogeneous distribution of ^{123}I-IPOS due to poor spatial resolution. Recently, we found that intratumoral heterogeneous distribution of radioactive IPOS might be imaged by using a single-photon-emission computed tomography (SPECT) scanner dedicated for small animal imaging, instead of planar gamma camera [13].

In this study, we aimed to clearly visualize heterogeneous intratumoral localization of ^{125}I-IPOS *in vivo* using fusion imaging methods of high-resolution SPECT and morphological imaging tests such as computed tomography (CT) and magnetic resonance imaging (MRI). And we tried to confirm the usefulness of these fusion images in the diagnosis of heterogeneous features inside tumors.

2. Materials and Methods

2.1. Synthesis of ^{125}I-IPOS. POS was overexpressed in *Escherichia coli* and purified, as previously reported [11]. Purified POS was dissolved in Tris-HCl buffer, pH 8.0. Sodium [^{125}I] iodine (629 GBq/mg as I) was purchased from Perkinelmer Japan. 3-Iodobenzoyl norbiotinamine (IBB) was prepared as described previously [14] and labeled with [125]I. ^{125}I-IPOS was obtained by the incubation of ^{125}I-IBB and POS for 1 hour. ^{125}I-IPOS was purified using a Sephadex G-50-filled spin column.

2.2. Animal Tumor Model. Five-week-old female C3H/He mice were purchased from Japan SLC (Hamamatsu, Japan). They were kept at 12/12 h dark-light cycles and were fed *ad libitum.* FM3A mouse breast cancer cells (5×10^6 cells) were subcutaneously implanted into a thigh of a mouse. These mice were used for the experiments 2 weeks after the inoculation. Implanted tumors in this model showed good affinity to IPOS in our previous study [13]. All animal experiments were carried out after the approval by the Ethical Committee for Animal Experiments of our institute.

2.3. Biodistribution of ^{125}I-IPOS. ^{125}I-IPOS (2.0 MBq/ 30 μg/0.2 mL) was intravenously injected into each mouse via its tail vein. The mice were sacrificed 24 hours after the injection because our previous study revealed that ^{125}I-IPOS accumulated well enough for SPECT imaging [11]. Whole-organ specimens were removed immediately and weighed, and their radioactivity was measured by a dose calibrator (IGC-7, Aloka, Tokyo, Japan) or an autowell gamma counter (ARC-380CL, Aloka).

2.4. Immunohistochemistry and Autoradiography of Excised Tumors. ^{125}I-IPOS (2.0 MBq/30 μg/0.2 mL) was intravenously injected into mice via their tail veins. Pimonidazole (60 mg/kg) was intravenously injected into these mice 1 h before the dissection. These mice were sacrificed 24 h after the injection of ^{125}I-IPOS. The excised tumors were embedded in OCT compound (Sakura Finetek Japan, Tokyo, Japan), frozen, and cut into 6 μm thick sections for hematoxylin-eosin (H&E) staining and fluorescent immunostaining of pimonidazole, and 20 μm thick sections for autoradiography (ARG) using a cryomicrotome (CM 3050S, Leica Instruments, Wetzlar, Germany). For fluorescent immunostaining of pimonidazole, FITC-conjugated mouse IgG₁ monoclonal antibody (Chemicon, Temecula, CA, USA) was treated according to the manufacture's protocol for pimonidazole staining. For ARG, the sliced tumor specimens were placed in contact with an imaging plate (MS2040, Fujifilm, Tokyo, Japan), and the exposed imaging plates were analyzed by an FLA-7000 reader (Fujifilm) and Multi-Gause ver. 3.0 software (Fujifilm).

2.5. SPECT/CT Imaging.

High dose of ^{125}I-IPOS (20 MBq/30 μ g/0.2 mL) was intravenously injected into 2 mice via their tail veins. The mice were anesthetized by the inhalation of isoflurane gas 24 hours after the injection. SPECT images were obtained using a SPECT/CT combined scanner dedicated for small animal imaging (NanoSPECT/CT, Bioscan, Washington, D.C., USA). This scanner had 4 detectors with tungsten multipinhole collimators (number of pinholes: 9, the diameter of pinhole: 1.4 mm). First, CT images were acquired by a continuous helical scanning method. The acquisition conditions were as follows: tube voltage: 45 keV, tube current: 177 μA. Then, SPECT images were obtained by a step-and-shoot helical scanning method. The energy window was set between 20 and 36 keV. The acquisition time was set to 5 min for each step. Six steps of 4 detectors, total 24 steps, covered 360 degrees.

The acquired image data of both CT and SPECT were reconstructed by using InVivoScope software (Bioscan). Filtered back-projection algorithms and ordered subset-expectation maximization ones were used for CT image data and for SPECT ones, respectively.

The excised tumor was also imaged using the same SPECT/CT scanner *ex vivo*. The SPECT acquisition time for single step was set to 10 min. Both *in vivo* and *ex vivo* SPECT images superimposed on CT images were compared with each other.

2.6. MR Imaging and Image-Fusion of SPECT and MRI.

High-dose ^{125}I-IPOS (20 MBq/30 μg/0.2 mL) was intravenously injected into 2 mice via their tail veins. The mice were anesthetized by mixed gas of isoflurane and nitrogen oxide 24 hours after the injection. After the anesthesia, the mice were put on the special bed that was designed for the fusion imaging of SPECT and MR imaging and immobilized by fastening their extremities to the bed. MR images were acquired using a 3.0T whole-body scanner (Signa HDx, GE Healthcare, Milwaukee, WI, USA) combined with a 3-turn solenoid coil with the internal diameter of 35 mm. The following pulse sequence of 2D fast spin echo was used: TR = 4,000 ms, effective TE = 60.7 ms, echo train length = 8. Field of view was set to 4 × 4 cm^2 with the matrix size of 256 × 192. Slice thickness was set to 1 mm. And the total acquisition time was 6 m 40 s. SPECT images were acquired as described above.

SPECT images were superimposed on obtained MR images so that images of markers attached on the cover of the special bed completely overlapped each other on both images.

3. Results

3.1. Biodistribution of ^{125}I-IPOS.

The biodistribution of ^{125}I-IPOS in FM3A-bearing mice 24 h after the injection is shown in Figure 1.

^{125}I-IPOS was well accumulated in FM3A tumors implanted in the thigh of mice. The uptake ratio of ^{125}I-IPOS in FM3A tumors was 4.3 ± 0.68% of administered dose/g (mean SD) The reticuloendothelial organs such as liver and

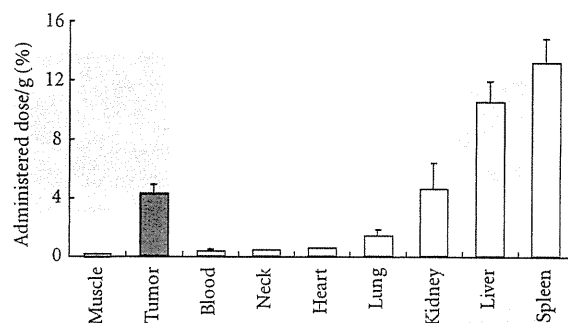Figure 1: Biodistribution of ^{125}I-POS in FM3A-bearing mice. Administration dose of ^{125}I-POS 2.0 MBq, POS: 30 μg, tumor weight: 0.3–2.3 g, tumor uptake 4.3% AD/g, T/B: 13.1%(n = 5).

spleen showed strong uptake of this probe whereas neck including thyroid gland and muscle showed weak uptake. As a result, tumor-to-blood ratio was as high as 13.1.

3.2. Immunohistochemistry and Autoradiography of Excised Tumors.

ARG tests revealed the heterogeneous ^{125}I-IPOS distribution in FM3A tumors (Figure 2). Fusion imaging of ARG and H&E staining indicated that ^{125}I-IPOS was distributed in viable areas. Fusion imaging of ARG and pimonidazole staining showed the intratumoral location of ^{125}I-IPOS partially overlapped with that of pimonidazole (arrows, Figure 2). But there was discrepancy between the intratumoral location of ^{125}I-IPOS and pimonidazole.

3.3. SPECT/CT Images of FM3A Tumors.

As high radioactivity must be accumulated in target tissues to obtain images with excellent spatial resolution, ^{125}I-IPOS with high radioactivity of 22 MBq was administered to each mouse, and *in vivo* SPECT/CT images were acquired. The obtained SPECT images successfully depicted the heterogeneous distribution of ^{125}I-IPOS in FM3A tumors with excellent resolution (Figure 3).

After the acquisition of *in vivo* SPECT images, tumors were excised and weighed and their radioactivity was measured. The radioactivities of both tumors were 0.68 MBq (0.93 g, 0.73 MBq/g) and 1.19 MBq (1.37 g, 0.87 MBq/g), respectively. Then *ex vivo* tumor images were obtained. As *ex vivo* images were obtained with longer acquisition time than *in vivo* ones and there were no surrounding tissues around the tumor tissues that cause scattering of emitted photons in *ex vivo* images, image quality of *ex vivo* images was superior to that of *in vivo* ones. However, *in vivo* images also rather well depicted the heterogeneous intratumoral distribution of ^{125}I-IPOS (Figure 3).

As for the fusion imaging of SPECT and CT, since the tissue contrast inside tumors on CT images was poor, fusion images failed to provide useful information about the features of uptake sites of ^{125}I-POS.

3.4. Fusion Images of SPECT and MRI.

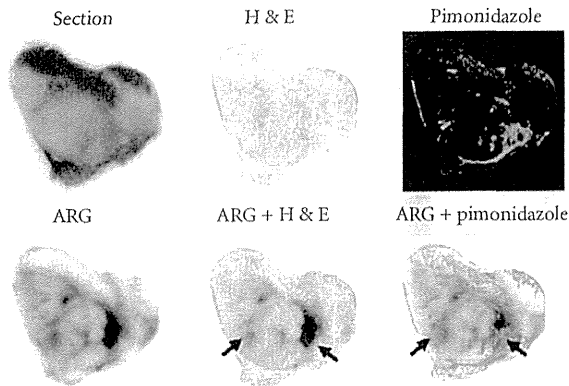MR images could provide more detailed tissue contrast than CT images. As

FIGURE 2: Intratumoral distribution of ^{125}I-POS, pimonidazole. Administration dose of ^{125}I-POS 2.0 MBq, POS: 30 μg, tumor weight: 0.3 g, tumor uptake 5.2%, slice thickness for ARG 20 μm, slice thickness for staining 6 μm.
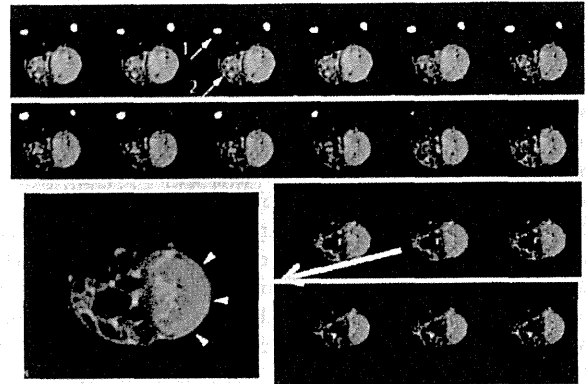

FIGURE 4: In vivo fusion imaging of intratumoral distribution of ^{125}I-POS and MR images. A representative image is enlarged. Arrows 1: markers, arrows 2: urinary bladder, and arrowheads: the tumor.
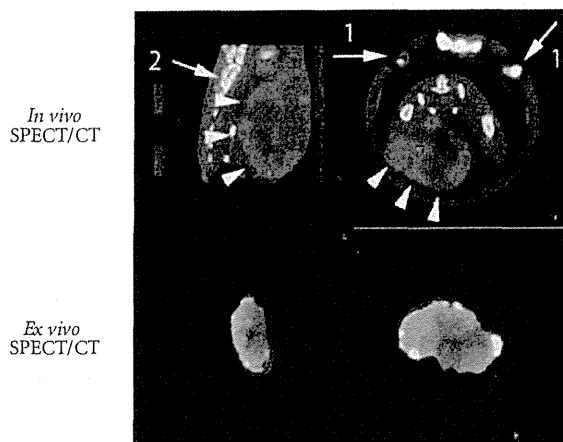

FIGURE 3: In vivo visualization of heterogeneous intratumoral distribution of POS by SPECT/CT. The comparison of in vivo SPECT images and ex vivo images. Upper raw: in vivo SPECT images, lower raw: ex vivo SPECT images, left column: sagittal sectional images, right column: axial sectional images. Arrows 1: markers for coregistration, arrows 2: vertebrae, and arrowheads: the tumor.

a result, the superimposition of SPECT images on MR images could give more information about the intratumoral distribution of ^{125}I-IPOS than that on CT images. Figure 4 shows the fusion images of ^{125}I-IPOS SPECT and MR images. As MR images are T2-weighted ones, high signal in the central area of the tumor suggests nonviable tumor tissues. And ^{125}I-IPOS does not accumulate in these high signal areas. SPECT-MR fusion images show that ^{125}I-IPOS is heterogeneously distributed in the low-signal area in the tumor, probably viable tumor areas.

4. Discussion

We have investigated the precise evaluation of intratumoral localization of HIF activity to establish strategies to optimize cancer treatment.

As the intratumoral distribution of ^{125}I-POS evaluated by ARG partially corresponded with that of pimonidazole, the accumulation of ^{125}I-POS in tumor tissues would be related with tumor hypoxia. The discrepancy can be explained by the facts that HIF activates in the milder hypoxic areas, compared with hypoxic areas with high affinity to pimonidazole [6]. Currently, some PET probes such as ^{18}F-fluoromisonidazole (FMISO), ^{18}F-fluoro-azomycinarabino-furanoside (FAZA), and ^{62}Cu-diacetyl-bis(N4-methylthiosemicarbazone) (ATSM) are under the clinical investigation [4]. As the intratumoral distribution of these probes directly depends on the oxygen partial pressure in tumor tissues, like pimonidazole, they accumulate well in severe hypoxic areas. On the other hand, it is expected that ^{125}I-POS distributes in the tumor according to HIF activity. Our previous study actually demonstrated by an immunohistological method that intratumoral distribution of ^{125}I-IPOS was well correlated with HIF activity [13].

But it is difficult to clearly visualize this heterogeneity in intratumoral localization of ^{125}I-IPOS in vivo.

To resolve this difficult problem, we first examined high-resolution SPECT to precisely depict intratumoral distribution of HIF activity. Then, the obtained SPECT images were superimposed on morphological images such as CT and MRI to add anatomical information to intratumoral distribution of HIF activity.

It is necessary to acquire a lot of counts to obtain high-resolution SPECT images [15]. For this purpose, it is required to accumulate high counts of radioactive compounds in target tissues or to acquire images for a long time. The acquisition time is usually limited by effects of longitudinal changes of biodistribution of radioactive compounds and those of the movement of animal bodies. Therefore, it would be better to consider a method to

accumulate a lot of radioactive compounds in target tissues. More accurately speaking, radioactivity concentration in the target tissues should be high.

We synthesized ^{125}I-IPOS with radioactivity concentration of as high as 100 MBq/mL and injected this high activity of ^{125}I-IPOS (20 MBq/30 μg/0.2 mL) into tumor-bearing mice. As a result, ^{125}I-IPOS could be accumulated in tumor tissues with average radioactivity concentration of 0.8 MBq/g. When these mice were acquired by a SPECT scanner dedicated for small animal imaging, heterogeneous intratumoral distribution of ^{125}I-IPOS was successfully imaged in vivo with the total acquisition time of 30 minutes.

After that, ex vivo SPECT images of excised tumors were obtained. In ex vivo imaging, acquisition time was longer. And statistical noise is reduced by the suppression of scattering and attenuation of gamma rays due to the removal of tissues surrounding a tumor. That is why the image quality of ex vivo SPECT images is likely to be superior to of that in vivo ones. Considering these factors, in vivo SPECT images were never inferior to ex vivo ones in the light of the visualization of intratumoral heterogeneity.

Our previous experimental study using ^{111}In reported that the radioactivity concentration larger than 0.2 MBq/mL was needed to image the heterogeneous distribution of radiopharmaceuticals in tissues [16]. Since the energy of photons emitted from ^{125}I is much lower than that from [111]In [17], radioactivity concentration higher than 0.2 MBq/mL would be required to depict the heterogeneous distribution in tissues by ^{125}I-labeled compounds. The radioactivity concentration of 0.8 MBq/g, which we obtained in this study, was high enough to visualize the heterogeneous distribution of ^{125}I-labeled compounds.

In the light of the energy of emitted photons and half-life, ^{123}I-labeled compounds are more suitable for clinical nuclear medicine tests than ^{125}I ones. But, to obtain SPECT images with excellent spatial resolution in small animal studies, radioactive probes with high radioactive concentration and specific radioactivity are required [16]. In our country, it is, however, very difficult to get Na[123]I with high specific radioactivity. That is why we used ^{125}I-labeled compounds in this study.

It is often difficult to evaluate the features of target tissues where radioactive compounds accumulated only by SPECT images due to the lack of anatomical information. The situation is same in the clinical practice. Therefore, super-imposition of SPECT images on morphological images such as CT and MRI is actively examined to settle this problem.

In this study, as images of ^{125}I-IPOS were obtained using a SPECT/CT combined scanner, the fusion images of SPECT and CT could be easily obtained using preinstalled software. The superimposition on CT images provided the information about the position of the uptake of ^{125}I-IPOS. But additional information about the pathological features of ^{125}I-IPOS uptake areas was poor because the tissue contrast of CT images was not excellent and the change of CT number inside tumors was minimal.

On the other hand, fusion imaging of SPECT and MRI took a lot of effort. As MR images could not be obtained using a combined scanner with SPECT, it was required

to image mice by putting them on a special bed with markers for coregistration [18]. Good tissue contrast of MRI, however, could provide important information about the features of tumor interiors. In this study, SPECT-MRI fusion images successfully suggested that ^{125}I-IPOS was distributed in mainly viable tumor tissues.

There are some problems that must be settled in SPECT-MRI fusion imaging: the accuracy of coregistration, the distortion of images, and so on. But SPECT-MRI fusion images can provide more useful information about the features of tumor interiors than SPECT-CT images. Therefore, SPECT-MRI fusion imaging should be more actively investigated.

The clinical application of fusion images of radioactive IPOS SPECT and morphological imaging tests, especially MRI, will be an important research project in the future. It is expected that the fusion images of radioactive IPOS SPECT and CT or MRI will contribute toward overcoming the resistance to cancer therapy such as radiotherapy and chemotherapy.

5. Conclusion

High-resolution SPECT images successfully demonstrated heterogeneous intratumoral distribution of ^{125}I-IPOS in vivo. The superimposition of SPECT images on CT images, more favorably MR images, would be useful to understand the features of heterogeneous intratumoral expression of HIF activity in vivo.

Conflict of Interests

The authors declare no conflict of interests.

Acknowledgments

References

[1] M. Chivukula, R. Bhargava, A. Brufsky, U. Surti, and D. J. Dabbs, "Clinical importance of HER2 immunohistologic heterogeneous expression in core-needle biopsies vs resection specimens for equivocal (immunohistochemical score 2+) cases," Modern Pathology, vol. 21, no. 4, pp. 363–368, 2008.

[2] K. Kubota, "From tumor biology to clinical PET: a review of positron emission tomography (PET) in oncology," Annals of Nuclear Medicine, vol. 15, no. 6, pp. 471–486, 2001.

[3] R. L. Wahl, L. E. Quint, R. D. Cieslak, A. M. Aisen, R. A. Koeppe, and C. R. Meyer, "'Anatometabolic' tumor imaging: fusion of FDG PET with CT or MRI to localize foci of increased activity," Journal of Nuclear Medicine, vol. 34, no. 7, pp. 1190–1197, 1993.

[4] A. R. Padhani, K. A. Krohn, J. S. Lewis, and M. Alber, "Imaging oxygenation of human tumours," *European Radiology*, vol. 17, no. 4, pp. 861–872, 2007.

[5] P. Vaupel and A. Mayer, "Hypoxia in cancer: significance and impact on clinical outcome," *Cancer and Metastasis Reviews*, vol. 26, no. 2, pp. 225–239, 2007.

[6] S. Kizaka-Kondoh and H. Konse-Nagasawa, "Significance of nitroimidazole compounds and hypoxia-inducible factor-1 for imaging tumor hypoxia," *Cancer Science*, vol. 100, no. 8, pp. 1366–1373, 2009.

[7] J. D. Chapman, "Measurement of tumor hypoxia by invasive and non-invasive procedures: a review of recent clinical studies," *Radiotherapy and Oncology*, vol. 20, no. 1, supplement, pp. 13–19, 1991.

[8] G. L. Semenza, "Intratumoral hypoxia, radiation resistance, and HIF-1," *Cancer Cell*, vol. 5, no. 5, pp. 405–406, 2004.

[9] H. Harada, S. Kizaka-Kondoh, and M. Hiraoka, "Optical imaging of tumor hypoxia and evaluation of efficacy of a hypoxia-targeting drug in living animals," *Molecular Imaging*, vol. 4, no. 3, pp. 182–193, 2005.

[10] T. Kuchimaru, T. Kadonosono, S. Tanaka, T. Ushiki, M. Hiraoka, and S. Kizaka-Kondoh, "In vivo imaging of HIF-active tumors by an oxygen- dependent degradation protein probe with an interchangeable labeling system," *PLoS ONE*, vol. 5, no. 12, article e15736, 2010.

[11] T. Kudo, M. Ueda, Y. Kuge et al., "Imaging of HIF-1-active tumor hypoxia using a protein effectively delivered to and specifically stabilized in HIF-1-active tumor cells," *Journal of Nuclear Medicine*, vol. 50, no. 6, pp. 942–949, 2009.

[12] M. Ueda, T. Kudo, Y. Kuge et al., "Rapid detection of hypoxia-inducible factor-1-active tumours: pretargeted imaging with a protein degrading in a mechanism similar to hypoxia-inducible factor-1α," *European Journal of Nuclear Medicine and Molecular Imaging*, vol. 37, no. 8, pp. 1566–1574, 2010.

[13] M. Ueda, T. Kudo, Y. Mutou et al., "Evaluation of ^{125}I-IPOS as a molecular imaging probe for hypoxia-inducible factor-1-active regions in a tumor: comparison among single-photon emission computed tomography/X-ray computed tomography imaging, autoradiography, and immunohistochemistry," *Cancer Science*, vol. 102, no. 11, pp. 2090–2096, 2011.

[14] C. F. Foulon, K. L. Alston, and M. R. Zalutsky, "Synthesis and preliminary biological evaluation of (3-iodobenzoyl) norbiotinamide and ((5-iodo-3-pyridinyl)carbonyl)norbiotinamide: two Radioiodinated biotin conjugates with improved stability," *Bioconjugate Chemistry*, vol. 8, no. 2, pp. 179–186, 1997.

[15] S. R. Cherry, J. A. Sorenson, and M. E. Phelps, *Image Quality in Nuclear Medicine*, Physics in Nuclear Medicine, Saunders, Philadelphia, Pa, USA, 2003.

[16] I. O. Umeda, K. Tani, K. Tsuda et al., "High resolution SPECT imaging for visualization of intratumoral heterogeneity using a SPECT/CT scanner dedicated for small animal imaging," *Annals of Nuclear Medicine*, vol. 26, no. 1, pp. 67–76, 2012.

[17] F. J. Beekman, D. P. McElroy, F. Berger, S. S. Gambhir, E. J. Hoffman, and S. R. Cherry, "Towards in vivo nuclear microscopy: iodine-125 imaging in mice using micropinholes," *European Journal of Nuclear Medicine*, vol. 29, no. 7, pp. 933–938, 2002.

[18] M. Yamaguchi, D. Suzuki, R. Shimizu et al., "Precise co-registration of SPECT and MRI for small animal imaging using a common animal bed with external references: visualization of macrophage distribution within inflammatory lymph nodes," in *Proceedings of 18th Meeting of the International Society for Magnetic Resonance in Medicine*, vol. 3963, 2010.

Initial experience of individualized chemoradiotherapy for superficial esophageal cancers based on the sentinel lymph node concept

Takuji Kaburagi · Hiroya Takeuchi · Hirofumi Fujii · Yoshiro Saikawa ·
Koji Murakami · Junichi Fukada · Naoyuki Shigematsu · Soji Ozawa ·
Nobutoshi Ando · Yuko Kitagawa

Abstract

Background Esophageal squamous cell carcinomas (ESCCs) invading the muscularis mucosae (T1a-MM) cause subclinical node metastasis in approximately 10 % of cases. When chemoradiotherapy (CRT) is administered to T1a-MM or deeper ESCC, prophylactic irradiation of areas with a risk of subclinical nodal metastasis may improve disease control. We had an opportunity for clinical observation of the status of lymph nodes in the patients whose hot spots in lymphoscintigraphy before CRT had been included within the irradiation field.

Methods We retrospectively investigated patients selected using following criteria: (1) cT1a-MM and cT1b without previous treatments, or pT1a-MM and pT1b cancers proved by previous endoscopic resections; (2) patients with neither clinical nodal nor distant metastasis; (3) patients whose hot spots detected by lymphoscintigraphy had been included within the irradiation fields. Lymphoscintigraphy had been examined with endoscopic injection of a radioisotope around the primary lesion before CRT.

Results Sixteen patients met the inclusion criteria. Of these patients [T1a-MM (4 cases), T1b-SM1 (2 cases), and T1b-SM2 (10 cases)], there were 9 definitive CRTs and 7 adjuvant CRTs after endoscopic resections. The median dose of irradiation was 60 Gy to the primary tumors and 46 Gy to the hot spots. All patients with definitive CRT achieved complete remission. At the median follow-up of 76.6 months, there was no lymph node recurrence.

Conclusions Prophylactic irradiation of the hot spots in lymphoscintigraphy may be effective. This result warrants further evaluation concerning the validity of irradiation field settings based on lymphoscintigraphic findings in patients with superficial ESCCs.

T. Kaburagi · H. Takeuchi (✉) · Y. Saikawa · Y. Kitagawa
Department of Surgery, Keio University School of Medicine,
35 Shinanomachi, Shinjuku-ku, Tokyo 160-8582, Japan
e-mail: htakeuchi@a6.keio.jp

H. Fujii
Functional Imaging Division, National Cancer Center Hospital
East, 6-5-1 Kashiwanoha, Kashiwa, Chiba 277-0882, Japan

K. Murakami · J. Fukada · N. Shigematsu
Department of Radiology, Keio University School of Medicine,
35 Shinanomachi, Shinjuku-ku, Tokyo 160-8582, Japan

S. Ozawa
Department of Surgery, Tokai University School of Medicine,
143 Kasuya, Isehara, Kanagawa 259-1193, Japan

N. Ando
Department of Surgery, Tokyo Dental College Ichikawa General
Hospital, 5-11-13 Sugano, Ichikawa, Chiba 272-8513, Japan

Introduction

According to the classification of esophageal cancer (10th edition) proposed by the Japan Esophageal Society [1], esophageal cancer in which tumor invasion does not extend beyond the submucosal layer is defined as "superficial carcinoma of the esophagus." With these relatively shallow squamous cell carcinomas, which are cancers that do not invade the lamina muscularis mucosae [T1a-EP and T1a-LPM according to the classification of esophageal cancer (10th edition) proposed by the Japan Esophageal Society], there is little risk of lymph node metastasis. However, tumors invading the lamina muscularis mucosae (T1a-MM)

🖉 Springer

cause subclinical lymph node metastasis in approximately 10 % of cases [2–4], and T1b cancers have lymph node metastasis in approximately 40 % of cases [2]. Therefore, T1a-EP or T1a-LPM cancers can be completely cured by endoscopic resection. However, for T1a-MM and deeper cancers, surgery or chemoradiotherapy (CRT) should be considered because of the risk of subclinical lymph node metastasis.

In Japan, esophagectomy with extended lymphadenectomy is considered to be the standard therapy for esophageal squamous cell carcinomas (ESCCs), but CRT is gaining popularity as a less invasive therapy. With respect to CRT for esophageal cancer, 5-fluorouracil (5FU) plus cisplatin (CDDP) is considered to be the standard concurrent chemotherapy [5, 6]; however, consensus concerning the extent of the irradiation field is lacking.

Lymphatic flow around the esophagus is multidirectional. The regions with potential for developing lymph node metastasis are widely spread from the cervical to abdominal areas [7–9]. There appears to be a risk of nodal recurrence with irradiation only to a primary tumor, and prophylactic nodal irradiation to these areas may improve disease control. However, it is known that a wide irradiation field increases the prevalence of adverse events. This is particularly true in case of late phase toxicity, where the use of wide fields sometimes leads to a fatal adverse event (e.g., radiation pneumonia, pleural effusion, pericardial effusion) [10, 11]. Moreover, in widespread areas with a risk of lymph node metastasis, prophylactic nodal irradiation to all these areas requires a very wide irradiation field and can lead to many adverse events.

We believe that if we can identify the areas where lymph node metastasis is likely to occur, we can establish suitable and relatively narrow irradiation fields for each patient. To identify the areas with a high prevalence of lymph node metastasis, the sentinel lymph node (SLN) concept appears to be important and useful. According to this concept, the first lymph node that receives lymphatic flow from a primary tumor is defined as the SLN, and the metastasis must occur first in the SLN if lymph node metastasis occurs.

We previously developed a radio-guided method for SLN mapping in gastrointestinal cancers [12] and reported on the validation of radio-guided SLN navigation in cN0 esophageal cancer [13]. In our previous study, SLNs were successfully identified by a gamma probe during surgery in 71 (95 %) of 75 patients with cT1N0M0 or cT2N0M0 primary esophageal cancers. The diagnostic accuracy based on SLN status was 94 % (67/71). In pT1 cancers, nodal metastases were confirmed as follows: SLN(−)/non-SLN(−) in 56.1 %, SLN(+)/non-SLN(−) in 23.6 %, SLN(+)/non-SLN(+) in 8.8 %, and SLN(−)/non-SLN(+) or undetected SLN in 10.5 % [13]. Therefore, approximately 80 % of pT1 patients had no lymph node metastasis or had lymph node metastasis only in SLNs. In addition, lymphoscintigraphy (LSG), which was assessed after injection of radioisotope into the submucosal layer around the primary tumor, showed the areas with uptake of radioisotope (hot spots). These hot spots were thought to be the areas containing SLNs.

LSG is well known as a non-invasive and clinically practical method of detecting radioactive SLNs. Previous studies demonstrated that not every radioactive node was visualized even in LSG [14, 15]. However, it is strongly expected that lymph nodes with positive LSG are probably a part of SLNs. In addition, a positive LSG response indicates that a considerable volume of lymph from the tumor flows into LSG-positive nodes (hot nodes) and that those nodes appear to be at a relatively high risk of subclinical metastasis.

Therefore, we hypothesized that optimized and individualized prophylactic nodal irradiation targeting SLNs would be effective in controlling superficial cN0 ESCC by CRT. In this study, we retrospectively investigated the outcome of lymph nodes in the patients whose hot spots in LSG before CRT had been included with in the irradiation fields.

Patients and methods

Patients

Of the patients with ESCCs treated by radiotherapy at Keio University Hospital (Tokyo, Japan) between January 2000 and December 2009, patients in this study were selected according to the following criteria: (1) histologically proven ESCC; (2) clinically diagnosed cT1a-MM or cT1bcN0cM0 cancers without any previous treatments of the primary lesions, or cancers pathologically diagnosed as pT1a-MM or pT1bcN0cM0 with previous endoscopic resection of the primary tumors; (3) patients whose hot spots detected by LSG before CRT were included within the irradiation field. Patients who had suffered from any advanced cancers within the previous 5 years were excluded from this study. LSG had been examined with endoscopic injection of radioisotope around the primary lesion before CRT.

In all patients, the depth and location of the tumor were assessed with esophagoscopy and barium swallow contrast study. Computed tomography (CT) from the neck to abdomen was used to confirm the absence of metastasis at regional lymph nodes and distant organs. Positron emission tomography (PET) was not performed routinely. In the patients who had previously undergone endoscopic resections, resected specimens were evaluated by pathological methods in accordance with Japanese guidelines.
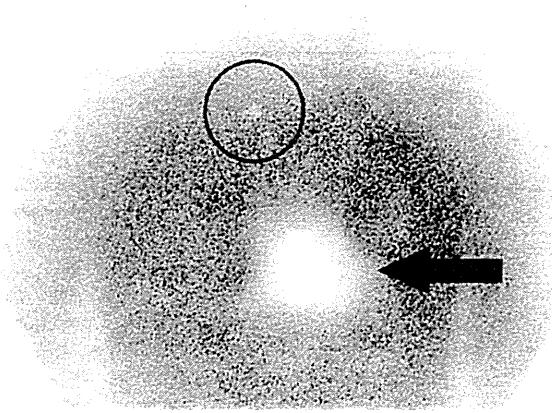
Fig. 1 Lymphoscintigraphy for sentinel lymph node mapping. The *black arrow* indicates uptake of radioisotope in the primary tumor. The *black circle* indicates a hot spot

Follow-up after CRT

In the first year after completion of CRT, esophagoscopy and CT (from neck to abdomen) were employed every 3 months. Those examinations were studied every 6 months after the 1st year and annually after the 5th year.

Lymphoscintigraphy procedure (SLN mapping)

Written informed consent concerning LSG for SLN mapping was obtained from all patients before procedures. A 0.5-ml volume of technetium-99m tin colloid solution (150 MBq) was injected into the submucosal layer at 4 sites around the primary tumor under endoscopic guidance [13]. In patients who had already undergone endoscopic resection of primary tumors, radioisotope solutions were injected around the scars. LSG was usually obtained 3–4 h after injection of the tracer (Fig. 1).

Radiologists evaluated the areas where hot spots were detected by LSG. Hot spots were classified into 5 areas: cervical (Ce), upper mediastinal (Ut), middle mediastinal (Mt), lower mediastinal (Lt), and abdominal (Ab).

Results

Sixteen patients were eligible for this study and were investigated retrospectively. Their clinical characteristics are summarized in Table 1. Fourteen patients were males and two were females. Median age was 66.5 years (range 58–77 years). The depth of tumor invasion was as follows: T1a-MM (4 patients), T1b-SM1 (2 patients), and T1b-SM2 (10 patients). Nine patients had never previously undergone endoscopic resection (definitive CRT group) and seven patients had previously undergone endoscopic

resection (adjuvant CRT group). In the latter, LSG was performed before endoscopic resection in 3 patients and after endoscopic resection in 4 patients. Hot spots in 12 patients (75.0 %) were detected by LSG. However, there was no evidence of hot spots in 4 patients (25.0 %).

5-FU/CDDP was administered as concurrent chemotherapy in 14 patients. Two patients received concurrent chemotherapies that did not include 5FU/CDDP. The first opted to receive outpatient treatment, and docetaxel monotherapy was selected as the concurrent chemotherapy. The second refused a long hospital stay, and CDDP monotherapy was chosen. The median total dose of irradiation delivered to the primary tumor was 60 Gy (range 34.2–60 Gy). Prophylactic nodal irradiation at a median total dose of 46 Gy (range 30–60 Gy) was delivered to the detected hot spots. In patient 3 in Table 1, wide prophylactic nodal irradiation (including the detected hot spots) at a total dose of 46 Gy was initially planned. However, after a dose of 30 Gy was administered, the irradiation field was narrowed down such that the detected hot spot was outside of the field because the patient experienced prolonged leukopenia, esophagitis, and fatigue. In patient 13 in Table 1, irradiation was initially planned at 50.4 Gy but was terminated at 34.2 Gy because of prolonged leukopenia. Prophylactic irradiation was not administered in 2 of 4 patients in whom hot spots were not observed on lymphoscintigraphy (patients 1 and 9 in Table 1). The entire mediastinum in patient 10 and the area between the middle mediastinum and the cardia in patient 14 were irradiated prophylactically.

The median follow-up time was 76.6 months (range 7.9–137.0 months). Nine patients achieved complete remission (CR) after definitive CRT. However, in 2 patients (nos. 2 and 3 in Table 1), minor local relapses of the primary tumors were observed. These patients underwent salvage endoscopic resections and survived without further relapse. Seven patients with adjuvant CRT survived without recurrence (Fig. 2). There was no recurrence of lymph node metastasis in any of the 16 patients. Severe adverse events due to long-term toxicity were not observed, nor were treatment-related deaths.

Discussion

Esophageal cancer frequently causes lymph node metastasis, which spreads from cervical to abdominal areas. Several reports demonstrated that esophagectomy with prophylactic three-field lymphadenectomy (cervical, mediastinal, and abdominal lymph nodes) undertaken to control subclinical lymph node metastasis may improve survival [16–18]. Thus, many Japanese surgeons consider radical esophagectomy with three-field lymphadenectomy as the standard therapy.

Table 1 Summary of the clinical characteristics of eligible patients

No.	Tumor location[a]	Depth of invasion[a]	Concurrent chemotherapy	Total irradiation dose (Gy/Fr)		Location of hot spots[b]	ER	Follow-up (months)	Outcome
				Primary	SLN				
1	Mt	cT1b-SM2	5FU/CDDP	60/30	46/23	No hot spot	–	137.0	No recurrence
2	MtLt	cT1a-MM	5FU/CDDP	60/30	30/15	Ce, Ut	–	130.0	No recurrence after salvage endoscopic resection
3	Mt	cT1a-MM	5FU/CDDP	60/30	46/23	Mt	–	127.6	No recurrence after salvage endoscopic resection
4	Mt	cT1b-SM2	5FU/CDDP	60/30	46/23	Ut, Mt	–	122.7	No recurrence
5	Lt	cT1b-SM2	5FU/CDDP	56/28	46/23	Ut	–	114.1	No recurrence
6	Mt	cT1b-SM2	5FU/CDDP	60/30	46/23	Ut	–	112.6	No recurrence
7	Mt	cT1a-MM	5FU/CDDP	60/30	40/20	Ut	–	81.5	No recurrence
8	UtCe	cT1b-SM2	5FU/CDDP	60/30	46/23	Ce, Mt	–	81.4	No recurrence
9	Mt	cT1b-SM1	5FU/CDDP	60/30	60/30	No hotspot	–	71.8	No recurrence
10	MtLt	pT1b-SM2	5FU/CDDP	60/30	60/30	No hotspot	+	43.6	No recurrence
11	Mt	pT1b-SM1	5FU/CDDP	58/29	48/24	Ut	+	23.7	No recurrence
12	LtAe	pT1b-SM2	5FU/CDDP	34.2/19	34.2/19	Ce	+	20.8	No recurrence
13	Lt	pT1b-SM2	Docetaxel	50/25	50/25	Ce, Ut	+	19.2	No recurrence
14	Mt	pT1a-MM	CDDP	60/30	60/30	No hot spot	+	17.3	No recurrence
15	Mt	pT1b-SM2	5FU/CDDP	50/25	50/25	Ut	+	17.0	No recurrence
16	Mt	pT1b-SM2	5FU/CDDP	60/30	46/23	Ut	+	7.9	No recurrence

ER a prior endoscopic resection

[a] According to the Guidelines for Clinical and Pathologic Studies on Carcinoma of the Esophagus (10th edition) [1]

[b] *Ce* cervical paraesophageal and supraclavicular area, *Ut* upper mediastinal area, *Mt* middle mediastinal area

Fig. 2 Summary of courses after chemoradiotherapy
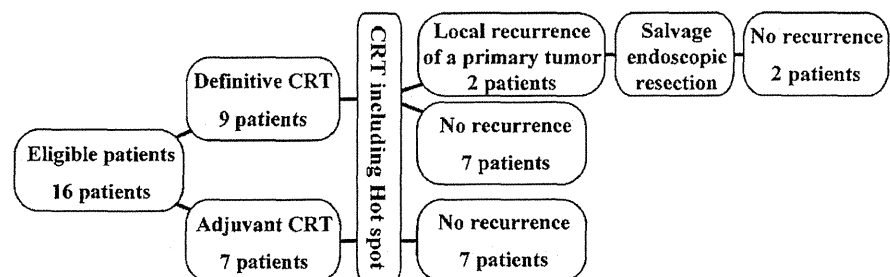
With regard to radiotherapy, there appears to be a risk of nodal recurrence if radiation is administered only to a primary site. Prophylactic nodal irradiation to these areas appears to perform an equivalent function to that of prophylactic lymphadenectomy and probably reduces recurrence of lymph node metastasis after CRT.

Kato et al. [19] reported on the findings of a phase II trial (JCOG9708) involving CRT on superficial esophageal cancer without prophylactic nodal irradiation. In this trial, the superior and inferior borders of the irradiation field were 3 cm beyond the primary tumor. CR was achieved in 87.5 %

of subjects, but recurrences of lymph node metastasis outside of the irradiation field were observed in 11.1 % of CR patients. If prophylactic nodal irradiation had been administered, the prevalence of these recurrences might have decreased. Additional studies have reported that wide prophylactic nodal irradiation can lead to good control of disease [20]. However, it is known that the use of a wide irradiation field results in many adverse events [10, 21].

Another phase II trial involving CRT for advanced esophageal cancer with wide prophylactic irradiation (JCOG9906) has been conducted [11]. In that trial, elective

nodal irradiation (40 Gy) of mediastinal and perigastric lymph nodes for all cases, cervical lymph nodes for an upper thoracic primary tumor and celiac lymph nodes for a lower thoracic primary tumor, was also undertaken. The authors found that grade-3 and grade-4 adverse events due to long-term toxicity occurred in 30.1 % of patients. Grade-3 and grade-4 late phase toxicities included: 13 % with esophagus toxicity, 16 % with pericardial effusion, 9 % with pleural effusion, and 4 % with radiation pneumonitis. Furthermore, adverse events that led to death were observed in 5.3 % of patients. Conversely, there were few adverse events due to late phase toxicity and no treatment-related death in the JCOG9708 clinical trial [19]. In summary, wide irradiation fields such as those used in the JCOG9906 study improved disease control but caused more adverse events because of late phase toxicities.

If we can identify where the first lymph node metastasis occurs for each case, suitable individual irradiation fields could be set up. The SLN theory appears to make this concept possible. We have reported on the validation of radio-guided SLN navigation for esophageal cancer [13].

In the present study, we investigated the patients whose hot spots detected by LSG, which probably contained SLNs, had been included within the irradiation field to assess the efficacy of prophylactic irradiation to SLNs. However, LSG did not detect hot spots in 4 cases. There are three potential reasons for this. First, SLNs might have been "hidden" by the shine-through effects of primary tumors because they were in close proximity to the primary tumor. Second, some SLNs might not have taken up sufficient amounts of the radioisotope for detection and thus LSG could not detect them. Third, macro-metastasis might exist at the true SLN and occlude original lymphatic flow, although it seems to be unlikely because this study included only cN0 patients. In consideration of the first reason, these 4 cases were considered eligible for inclusion in the present study. Including these 4 cases, recurrence of lymph node metastasis was not observed in any of the 16 patients.

This observational study was to clarify the status of some SLNs that were depicted on lymphoscintigraphic images. These lymph nodes resulted in no recurrence after performing chemotherapy and radiotherapy. It is unknown, however, (1) whether LSG had detected all SLNs in each patient, (2) which lymph nodes had had metastases at the time of CRT, and (3) whether the outcome would have changed if administering chemotherapy alone. Therefore, our study does not support an immediate use of modified CRT in which radiotherapy planning is based on the results of LSG.

In conclusion, the present study suggested that prophylactic irradiation to the hot spots detected by LSG may be effective in controlling superficial cancers of the esophagus. This result warrants further evaluation concerning the

validity of irradiation field settings based on lymphoscintigraphic findings in patients with superficial ESCCs. Moreover, if irradiation of the hot spots is effective, we can select the cases in which the irradiation field can be narrowed without increasing the risk of lymph node recurrence.

Recently, some research teams have reported on the utility of single-photon emission computed tomography/computed tomography (SPECT/CT) for SLN mapping in various malignancies [22]. They found that SPECT/CT for SLN mapping brought precise localization with three-dimensional imaging. Application of SPECT/CT to SLN mapping may improve detection and localization. It could also help in the development of treatments based on the SLN concept such as that used in the present study.

References

1. Japan Esophageal Society. Japanese classification of esophageal cancer, tenth edition: part 1. Esophagus. 2009;6:1–25.
2. Kodama M, Kakegawa T. Treatment of superficial cancer of the esophagus: a summary of responses to a questionnaire on superficial cancer of the esophagus in Japan. Surgery. 1998;123:432–9.
3. Makuuchi H, Shimada H, Chino O, Kise Y. Long term prgnosis of m3, sm1 cancer of the esophagus—comparison between EMR and radical surgery cases. Stomach Intestine. 2002;37:53–63.
4. Oyama T, Miyata Y, Shimatani S, Tomori A, Hotta K, Yoshida M. Lymph nodal metastasis m3, sm1 esophageal cancer. Stomach Intestine. 2002;37:71–4.
5. Cooper JS, Guo MD, Herskovic A, Macdonald JS, Martenson JA Jr, Al-Sarraf M, et al. Chemoradiotherapy of locally advanced esophageal cancer: long-term follow-up of a prospective randomized trial (RTOG 85-01). Radiation Therapy Oncology Group. JAMA. 1999;281:1623–7.
6. Minsky BD, Pajak TF, Ginsberg RJ, Pisansky TM, Martenson J, Komaki R, et al. INT 0123 (Radiation Therapy Oncology Group 94-05) phase III trial of combined-modality therapy for esophageal cancer: high-dose versus standard-dose radiation therapy. J Clin Oncol. 2002;20:1167–74.
7. Ando N, Ozawa S, Kitagawa Y, Shinozawa Y, Kitajima M. Improvement in the results of surgical treatment of advanced squamous esophageal carcinoma during 15 consecutive years. Ann Surg. 2000;232:225–32.
8. Igaki H, Kato H, Tachimori Y, Daiko H, Fukaya M, Yajima S, et al. Clinicopathologic characteristics and survival of patients with clinical Stage I squamous cell carcinomas of the thoracic esophagus treated with three-field lymph node dissection. Eur J Cardiothorac Surg. 2001;20:1089–94.
9. Tsurumaru M, Kajiyama Y, Udagawa H, Akiyama H. Outcomes of extended lymph node dissection for squamous cell carcinoma of the thoracic esophagus. Ann Thorac Cardiovasc Surg. 2001;7:325–9.
10. Ishikura S, Nihei K, Ohtsu A, Boku N, Hironaka S, Mera K, et al. Long-term toxicity after definitive chemoradiotherapy for squamous cell carcinoma of the thoracic esophagus. J Clin Oncol. 2003;21:2697–702.

11. Kato K, Muro K, Minashi K, Ohtsu A, Ishikura S, Boku N, et al. Phase II study of chemoradiotherapy with 5-fluorouracil and cisplatin for stage II–III esophageal squamous cell carcinoma: JCOG trial (JCOG 9906). Int J Radiat Oncol Biol Phys. 2010;81:684–90.

12. Kitagawa Y, Fujii H, Mukai M, Kubota T, Ando N, Watanabe M, et al. The role of the sentinel lymph node in gastrointestinal cancer. Surg Clin North Am. 2000;80:1799–809.

13. Takeuchi H, Fujii H, Ando N, Ozawa S, Saikawa Y, Suda K, et al. Validation study of radio-guided sentinel lymph node navigation in esophageal cancer. Ann Surg. 2009;249:757–63.

14. Nakahara T, Kitagawa Y, Takeuchi H, Fujii H, Suzuki T, Mukai M, et al. Preoperative lymphoscintigraphy for detection of sentinel lymph node in patients with gastric cancer—initial experience. Ann Surg Oncol. 2008;15:1447–53.

15. Uenosono Y, Arigami T, Yanagita S, Kozono T, Arima H, Hirata M, et al. Sentinel node navigation surgery is acceptable for clinical T1 and N0 esophageal cancer. Ann Surg Oncol. 2011;18:2003–9.

16. Isono K, Sato H, Nakayama K. Results of a nationwide study on the three-field lymph node dissection of esophageal cancer. Oncology. 1991;48:411–20.

17. Lerut T, De Leyn P, Coosemans W, Van Raemdonck D, Scheys I, LeSaffre E. Surgical strategies in esophageal carcinoma with emphasis on radical lymphadenectomy. Ann Surg. 1992;216:583–90.

18. Nishihira T, Hirayama K, Mori S. A prospective randomized trial of extended cervical and superior mediastinal lymphadenectomy for carcinoma of the thoracic esophagus. Am J Surg. 1998;175:47–51.

19. Kato H, Sato A, Fukuda H, Kagami Y, Udagawa H, Togo A, et al. A phase II trial of chemoradiotherapy for stage I esophageal squamous cell carcinoma: Japan Clinical Oncology Group Study (JCOG9708). Jpn J Clin Oncol. 2009;39:638–43.

20. Onozawa M, Nihei K, Ishikura S, Minashi K, Yano T, Muto M, et al. Elective nodal irradiation (ENI) in definitive chemoradiotherapy (CRT) for squamous cell carcinoma of the thoracic esophagus. Radiother Oncol. 2009;92:266–9.

21. Kumekawa Y, Kaneko K, Ito H, Kurahashi T, Konishi K, Katagiri A, et al. Late toxicity in complete response cases after definitive chemoradiotherapy for esophageal squamous cell carcinoma. J Gastroenterol. 2006;41:425–32.

22. Vermeeren L, van der Ploeg IM, Olmos RA, Meinhardt W, Klop WM, Kroon BB, et al. SPECT/CT for preoperative sentinel node localization. J Surg Oncol. 2010;101:184–90.

Contents lists available at SciVerse ScienceDirect

Lung Cancer

Evaluation for local failure by ^{18}F-FDG PET/CT in comparison with CT findings after stereotactic body radiotherapy (SBRT) for localized non-small-cell lung cancer

Atsuya Takeda [a], Etsuo Kunieda [b], Hirofumi Fujii [c,*], Noriko Yokosuka [d], Yousuke Aoki [a], Yoshikazu Oooka [a], Yohei Oku [a], Toshio Ohashi [a,e], Naoko Sanuki [a], Tomikazu Mizuno [a], Yukihiko Ozawa [d]

[a] Department of Radiology, Ofuna Chuo Hospital, Japan
[b] Department of Radiation Oncology, Tokai University, Japan
[c] Functional Imaging Division, Research Center for Innovative Oncology, National Cancer Center Hospital East, Japan
[d] Department of Radiology, Yuai Clinic, Japan
[e] Department of Radiology, Keio University, Japan

ARTICLE INFO

ABSTRACT

Purpose: Stereotactic body radiotherapy (SBRT) is the standard care for medically inoperable early non-small-cell lung cancer (NSCLC). However, it can be difficult to differentiate local recurrence from non-recurrence radiation-induced lung opacity. We retrospectively assessed ^{18}F-FDG PET/CT to detect local recurrence after SBRT for NSCLC.
Methods: Between 2005 and 2011, 273 NSCLCs in 257 patients were treated with SBRT. Prescribed doses were 50 Gy and 40 Gy per 5 fractions for peripheral and central lesions, respectively. Tri-monthly follow-up CT scans were acquired. ^{18}F-FDG PET/CT scans were scheduled for screening at one year after SBRT or when recurrence was highly suspected. The dual-time-point maximum standardized uptake values (SUVmaxs) and their retention indexes (RIs) were obtained.
Results: A total of 214 ^{18}F-FDG PET/CT scans were obtained for 164 localized NSCLC tumors in 154 patients. The median follow-up period was 24.9 months (range: 6.3–72.1). Among these, 21 scans of 17 tumors were diagnosed as local recurrence. The median SUVmaxs on early and late images of recurrence and their RI were 5.0 (range: 3.2–10.7), 6.3 (range: 4.2–13.4), and 0.20 (range; 0–0.41), respectively. These were significantly higher than the respective values of non-recurrence images of 1.8 (range: 0.5–4.6), 1.7 (range: 0.5–6.1), and 0.00 (range: −0.37–0.41) (all $p < 0.05$). For SUVmaxs on early and late images, optimal thresholds were identified as 3.2 and 4.2. Using each threshold, the sensitivity and specificity were 100% and 96–98%, respectively. CT findings were classified into ground-glass opacity ($N = 9$), scar or fibrotic change ($N = 96$), consolidation with air-bronchogram ($N = 34$), consolidation only ($N = 22$), and nodule ($N = 17$); the respective numbers of recurrence were 0, 0, 1, 3, and 17.
Conclusion: SUVmaxs of ^{18}F-FDG PET/CT could detect local recurrence after SBRT for localized NSCLC. In contrast, CT scan results had a limited ability to diagnose local recurrence.

1. Introduction

Stereotactic body radiotherapy (SBRT) has shown good clinical results comparable to those with surgery, and has excellent therapeutic effects and mild adverse effects [1]. Currently, SBRT is the standard care for medically inoperable stage I NSCLC. Moreover, SBRT is under investigation to determine whether it can become a standard of care, even for the operable or high-risk operable early stages of NSCLC.

In the National Comprehensive Cancer Network (NCCN) guidelines for clinical follow-up after treatment of stage I–IV NSCLC patients, contrast-enhanced chest CT every 4–6 months for 2 years is recommended [2]. However, diagnoses of local recurrences during the follow-up after SBRT are often difficult. Chest CT may lead to misdiagnosis when evaluating tumor control [3,4]. Radiation-induced lung opacities (RILO) following SBRT may not precisely correspond to the planning target volumes (PTV) and may dynamically vary both in shape and location during the follow-up period [5]. Radiation fibrosis is often observed and may be difficult to distinguish from tumor recurrence, even at a chronic phase after SBRT [3,4].

* Corresponding author at: Functional Imaging Division, Research Center for Innovative Oncology, National Cancer Center, 6-5-1 Kashiwanoha, Kashiwa 277-8577, Japan. Tel.: +81 4 7134 6831; fax: +81 4 7134 6832.
E-mail address: fujii-rad@umin.org (H. Fujii).

For the current investigation, our primary aim was to verify the clinical utility of ^{18}F-FDG PET/CT to diagnose local recurrence by defining threshold values for maximum standardized uptake value (SUVmax) using a single PET/CT combined scanner. Our secondary aim was to verify the clinical utility of CT to diagnose local recurrence by classifying the CT findings of RILO into categories and to evaluate correlations between CT findings and ^{18}F-FDG PET/CT SUVmaxs.

2. Materials and methods

2.1. Patients and study design

Between April 2005 and August 2011, we treated 273 localized lung cancers in 257 patients with SBRT in our institution. They included 16 patients who had 2 metachronous lesions and were treated with SBRT twice, each at different times. After SBRT, patients underwent ^{18}F-FDG PET/CT for screening or for detailed checks for recurrence. The minimum follow-up time after post-treatment ^{18}F-FDG PET/CT was 2 months for patients regarded as having no recurrence and was 6 months for patients with suspected recurrence. All patients provided written informed consent for treatment and follow-up. Yuai Clinic and Ofuna Chuo Hospital Review Boards approved this study (2011-008).

2.2. Treatment

Specific details for SBRT treatment were described previously [6,7]. In brief, for radiation treatment planning CT, long-scan-time CT was performed to directly visualize the internal target volume (ITV) while immobilizing the patient in a vacuum pillow [6]. After ascertaining that breathing-related tumor movement was <1 cm, scan period was set to exceed the duration of one respiratory cycle for all patients. The PTV was determined by adding a margin of 6–8 mm to the ITV. The prescribed dose was defined as 80% of the maximal dose in the PTV, and the leaf margins were modified to ensure that the PTV would be included in the 80% isodose surface. The dynamic conformal multiple arc therapy was used with the prescribed doses of 50 Gy or 40 Gy per 5 fractions for peripherally located primary lesions or centrally located primary lesions, respectively [7]. The biologically effective doses assuming alpha/beta ratios of 10 Gy (BED10) for the prescribed doses of 40 Gy and 50 Gy in 5 fractions at the periphery of the PTV were 72 Gy and 100 Gy, respectively, and those at the isocenter were 100 Gy and 141 Gy, respectively.

2.3. Follow-up

Our follow-up procedures were described previously [3]. CT scans were performed at one month after SBRT and then at 3-month intervals during the first two years. Subsequent follow-up CT scans were obtained at 4–6-month intervals. One year after SBRT, ^{18}F-FDG PET/CT was scheduled on a single scanner to differentiate local recurrence from RILO and to screen out other metastases. Additionally, ^{18}F-FDG PET/CT was performed when any recurrences were suspected.

2.4. Computed tomography

We typically performed non-contrast-enhanced CT with high-resolution CT. However, contrast-enhanced CT was used for the tumors adjacent to vessels. CT findings of RILO were differentiated based on a consensus decision between a diagnostic radiologist (T.M.) and a radiation oncologist (A.T.). RILO findings were grouped

into categories. In addition, these were divided into either recurrent or non-recurrent RILO findings after the final diagnosis.

2.5. ^{18}F-FDG PET/CT

After fasting for 6 h, 3.5 MBq/kg b.w. ^{18}F-FDG was intravenously injected only if the patient's blood sugar level was lower than 200 mg/dl. Images were obtained using a single PET/CT combined scanner (Eminence-SOPHIA, Shimadzu, Kyoto, Japan). Early and delayed images were acquired at 60 and 120 min after injection. For the PET scan, emission image data from the eyes to mid-thighs were continuously acquired for approximately 20 min.

Lesions on the reconstructed sectional images were evaluated visually and quantitatively using SUVmax inside a volume of interest (VOI). The SUVmax was calculated as: [(maximum activity in VOI)/(volume of VOI)]/[(injected FDG dose)/(patient weight)].

We also calculated the retention index (RI) of each nodular lesion as follows: (SUVmax in the VOI on late image – SUVmax in the VOI on early image)/(SUVmax in the VOI on early image).

2.6. Diagnosis of local recurrence

Local control was defined for the following two conditions: (1) no evidence of recurrence on a follow-up CT scan at least two months after negative evaluations on both CT and ^{18}F-FDG-PET; and (2) no evidence of recurrence on two sequential CT scans over a 6-month period if undeniable findings of recurrence were indicated on either modality.

Local recurrence was diagnosed by pathological confirmation or defined as an increase of >25% in the cross-sectional tumor size on successive CT scans at least three times over a 6-month period. The date of local recurrence was defined as the date when an increase in tumor size or an abnormal FDG accumulation was suggested for the first time.

2.7. Statistical analysis

The variables of interest were SUVmaxs for the different RILO groups and recurrent or non-recurrent lesions. A Kruskal–Wallis test was used to compare differences in SUVmaxs among the RILO groups and recurrent lesions. A Steel–Dwass test was used to test for inter-group differences. P-values of <0.05 were considered significant.

The diagnostic performance of SUVmaxs and the RI was assessed by receiver-operating characteristic (ROC) curves and the total area under the curve (AUC). Optimal thresholds were determined by calculating minimum balanced error rates (BER). The 95% confidence interval (CI) for sensitivity, specificity and AUC were calculated. Analyses were performed using IBM SPSS Statistics 20.0 (IBM, Inc., Armonk, NY, USA).

3. Results

There were 257 patients with NSCLC treated with SBRT between April 2005 and August 2011. Among these patients, the total number of ^{18}F-FDG PET/CT scans using a single PET/CT combined scanner was 214 for 154 patients (60.0%) with 164 tumors: once for 120 patients; twice for 40 patients; three times for two patients; and four times for two patients. The purposes for these scans were screenings (N = 155) and detailed checks for recurrence (N = 59). The median ^{18}F-FDG PET/CT scan period after SBRT was 12.8 months (range: 3.5–52.5 months). The median follow-up period after SBRT was 24.9 months (range: 6.3–72.1 months). The reasons for ineligibility of the remaining 103 patients were: ^{18}F-FDG PET/CT done with other scanners (N = 5); patients' refusals (N = 30); lost to follow-up (N = 23), death or obvious recurrence

Table 1

Tumor characteristics.

	Recurrent tumors	Non-recurrent tumors
No. of tumors	17	147
No. of FDG-PET/CT scans	21	193
Median follow up duration	22.1 (6.3–57.5)	29.1 (9.0–72.1)
Median scanned period from SBRT	12.8 (5.7–57.1)	12.8 (3.5–52.5)
Median recurrent diagnosis period	12.3 (3.3–25.1)	–
Median age (range)	81 (68–90)	78 (55–91)
Male/female	14/3	101/46
Operability: yes/no	3/14	30/117
Median maximum diameter (cm)	3.5 (1.7–5.2)	2.4 (0.5–8.5)
ITV (ml)	23.8 (2.4–79.4)	7.6 (0.5–314.1)
PTV (ml)	69.2 (15.2–164.7)	32.2 (7.3–363.1)
T stage		
T1a	2	63
T1b	5	39
T2	7	38
T3	0	2
T4	3	5
Histology		
Adenocarcinoma	2	49
Squamous cell cancer	7	25
Unclassified NSCLC	1	13
Histologically unproved	7	60
Tumor opacity		
Solid	17	127
GGO	0	5
GGO with solid	0	15
Location: central/peripheral	8/9	46/101
Total dose: 50 Gy/40 Gy	10/7	123/24

Abbreviations: ITV, internal target volume; PTV, planning target volume; GGO, ground-glass opacity.

within 1 year ($N = 24$); follow-up of <1 year with no suspicion of recurrence ($N = 21$). The characteristics of the tumors are shown in Table 1. During follow-ups, 17 tumors were diagnosed as local recurrence. Three recurrences were proved by biopsy and the other 14 were diagnosed based on their enlargements on successive CT images. Among the 17 patients with recurrent tumors, ^{18}F-FDG PET/CT was acquired once for 13 patients and twice for four patients within six months before a diagnosis of recurrence. Thus, 21 ^{18}F-FDG PET/CT scans were of recurrent tumors.

In the latest follow-up, among 3 patients with pathologically confirmed recurrence, 2 patients had no evidence of disease following salvage SBRT or conventional radiotherapy. The other patient died of lung cancer. For all the 14 patients with clinically diagnosed local recurrence, the tumors' size continued increasing till last follow-up. They died of lung cancer. The median interval between the dates of last ^{18}F-FDG PET/CT and death was 13.6 (range: 6.5–42.2) months.

3.1. ^{18}F-FDG PET/CT SUVmaxs to diagnose recurrence

The median SUVmaxs on early images of recurrent ($N = 21$) and non-recurrent lesions ($N = 193$) were 5.0 (range: 3.2–10.7) and 1.8 (range: 0.5–4.6), respectively. Those on late images were 6.3 (range: 4.2–13.4) and 1.7 (range: 0.5–6.1), respectively. The RI's were 0.20 (range: 0.00–0.41) and 0.00 (range: −0.37–0.41), respectively. The dual-time-point SUVmaxs on both early and late images and their RI were significantly higher than those of non-recurrent lesions ($p < 0.05$). The median blood glucose level (mg/dl) was 98 (range: 65–189). Only eight patients with non-recurrent lesions had blood sugar levels exceeding 150 mg/dl.
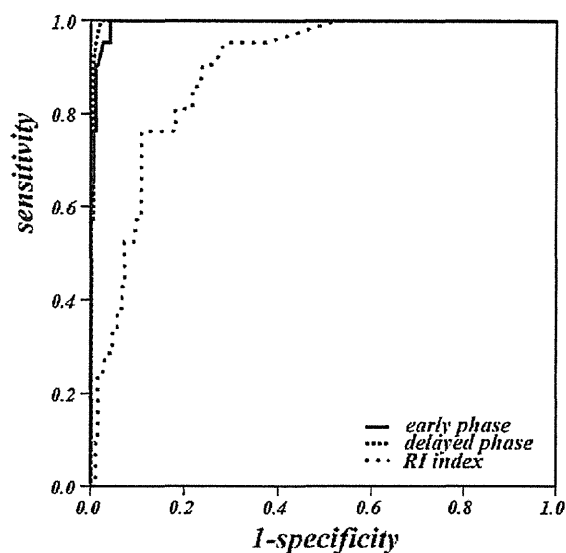

Fig. 1. Receiver-operating characteristic (ROC) curves. Each endpoint indicates local recurrence. Dotted line, gray line, and black line are the ROC curves for maximum standardized uptake values (SUVmax) on early images, late images, and retention index, respectively. For the SUVmaxs on early images, the optimal threshold was determined to be 3.7–3.9 and the sensitivity and specificity (=1 − false positive proportion) were 88% and 99%, respectively. For the SUVmaxs on late images, the threshold was 4.5–4.9 with a sensitivity and specificity of 88% and 100%, respectively. For the retention index, the threshold was 0.064–0.072 with a sensitivity and specificity of 88% and 67%, respectively.

3.2. Threshold SUVmaxs for distinguishing recurrent lesions from non-recurrence

ROC curves used to differentiate lesion recurrence by dual-time-point SUVmaxs and their RI are shown in Fig. 1. The corresponding outcomes are shown in Table 2. The AUCs for early and late images were not statistically different from each other, but were statistically greater than those for the RI. Regarding the SUVmaxs on early and late images, the optimal thresholds were determined to be 3.2 and 4.2, respectively. The sensitivity and specificity with 95% CI for the optimal threshold on early images were 1.00 (1.00–1.00) and 0.96 (0.93–0.99), and those on late images were 1.00 (1.00–1.00) and 0.98 (0.96–1.00), respectively (Table 2).

Fig. 2 shows recurrence or non-recurrence based on SUVmaxs. In the graphs for the dual-time-point SUVmaxs images, SUVmaxs
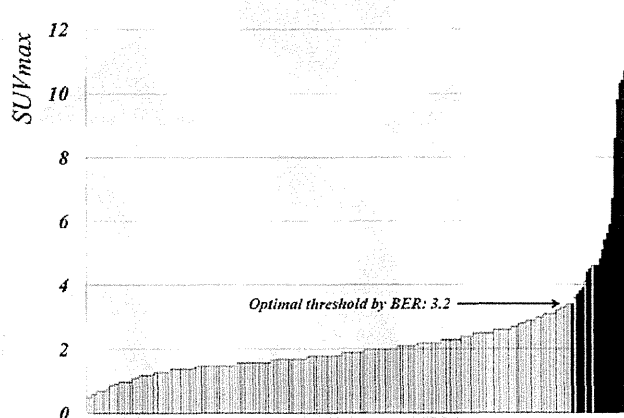

Fig. 2. Bar-code profiles that show recurrence or non-recurrence based on maximum standardized uptake values (SUVmax) on an early image. White and black bars represent non-recurrence and recurrence, respectively.

Table 2

Median and ranges of SUVmax in early and late image and RI.

	No. of lesions	Early image	Late image	Retention index
All non-recurrent opacities	193	1.8 (0.5–4.6)	1.7 (0.5–6.1)	0.00 (−0.37–0.41)
Ground-glass opacity	9	1.4 (0.9–2.1)	1.6 (0.8–1.9)	0.00 (−0.23–0.36)
Scar or fibrosis	96	1.7 (0.5–3.4)	1.6 (0.5–3.5)	−0.02 (−0.28–0.41)
Consolidation with air bronchogram	33	2.1 (0.7–3.2)	2.1 (0.6–3.9)	0.00 (−0.29–0.25)
Consolidation only	19	2.5 (1.4–4.6)	2.5 (1.3–6.1)	0.04 (−0.37–0.40)
Nodule	36	1.8 (0.7–4.1)	1.7 (0.7–4.4)	0.00 (−0.36–0.29)
Recurrence	21	5.0 (3.2–12.5)	6.3 (4.2–17.4)	0.20 (0.00–0.41)
Optimal threshold determined by BER		3.2	4.2	0.067
Sensitivity + specificity		1.00 + 0.96	1.00 + 0.98	0.95 + 0.72
ROC (AUC) (95% CI)		0.995 (0.988–1.000)	0.997 (0.992–1.000)	0.890 (0.835–0.945)
Sensitivity (95% CI): cut-off SUVmax =		3.2	1.00 (1.00–1.00)	1.00 (1.00–1.00)
	3.7	0.91 (0.78–1.00)	1.00 (1.00–1.00)	–
	4.2	0.76 (0.58–0.94)	1.00 (1.00–1.00)	–
	4.7	0.57 (0.36–0.78)	0.81 (0.64–0.98)	–
Specificity (95% CI): cut-off SUVmax =	3.2	0.96 (0.93–0.99)	0.93 (0.90–0.97)	–
	3.7	0.99 (0.98–1.00)	0.96 (0.94–0.99)	–
	4.2	1.00 (0.98–1.00)	0.98 (0.96–1.00)	–
	4.7	1.00 (1.00–1.00)	1.00 (0.98–1.00)	–

Abbreviations: No., number; ROC (AUC), the total area under the curve in receiver-operating characteristic curve; CI, confidence interval; SUVmax, the maximum standardized uptake value.

for recurrence and non-recurrence were sharply divided and the overlap ranges were small.

3.3. CT opacity of primary lesions following SBRT and diagnosis of recurrence

CT findings of RILO were grouped into the following 5 categories (Fig. 3): ground-glass opacity (GGO) ($N = 9$); scar or fibrotic change ($N = 96$); consolidation with air-bronchogram ($N = 34$) consolidation only ($N = 22$); and nodule ($N = 53$). Among these categories, the numbers of recurrent cases were, respectively, 0 (0%), 0 (0%), 1 (2.9%), 3 (13.6%), and 17 (32.1%). The median dual-time-point SUVmaxs and their RI's are shown in Table 2. The distributions of SUVmaxs for the non-recurrent opacities and recurrent lesions are shown in Fig. 4. The dual-time-point SUVmaxs and the RI were significantly different among non-recurrent opacities and

recurrent lesions ($p < 0.05$). From an analysis of multiple comparisons among factors, the dual-time-point SUVmaxs images and the RI of recurrent lesions were significantly higher than all of the non-recurrent opacities ($p < 0.05$), except for the RI for consolidation.

4. Discussion

Detecting local recurrence is essential for the evaluation of treatment outcome as well as clinical management, since it can lead to optimal and immediate treatment. Salvage surgery [8], cryoablation, radiofrequency ablation, or repeat SBRT [9] are often feasible and should be considered. Additionally, the procedures should be minimally invasive because they are often elderly and have co-morbidity.
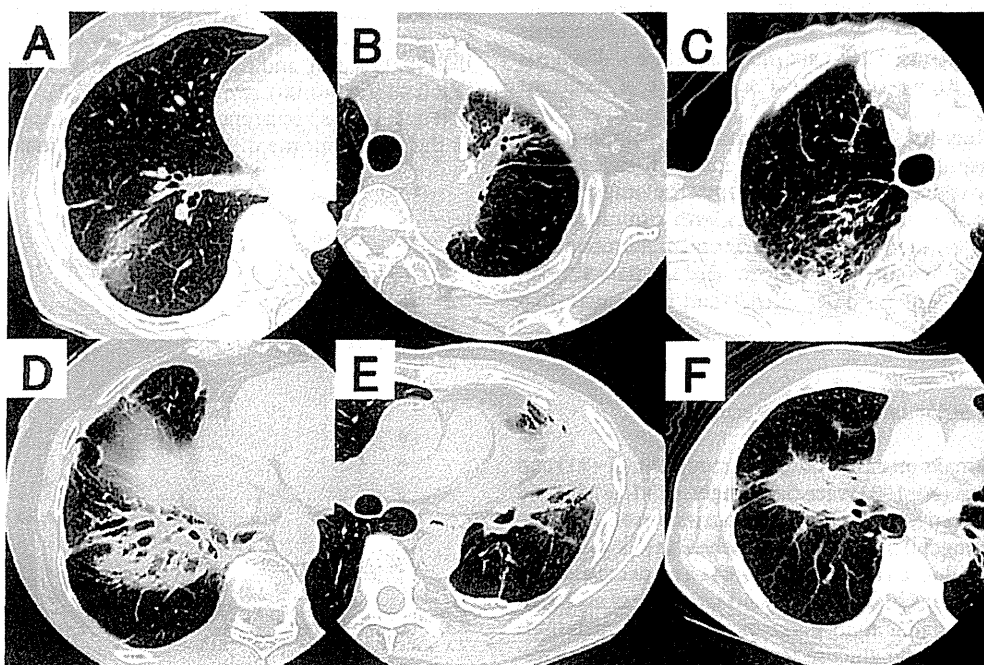

Fig. 3. Typical CT images of radiation-induced lung opacities. (A) Ground glass opacity (GGO), (B) scar, (C) fibrous change, (D) consolidation with air-bronchogram (AB), (E) consolidation only, (F) nodular opacity. All representative radiation-induced lung opacities were not associated with recurrence.
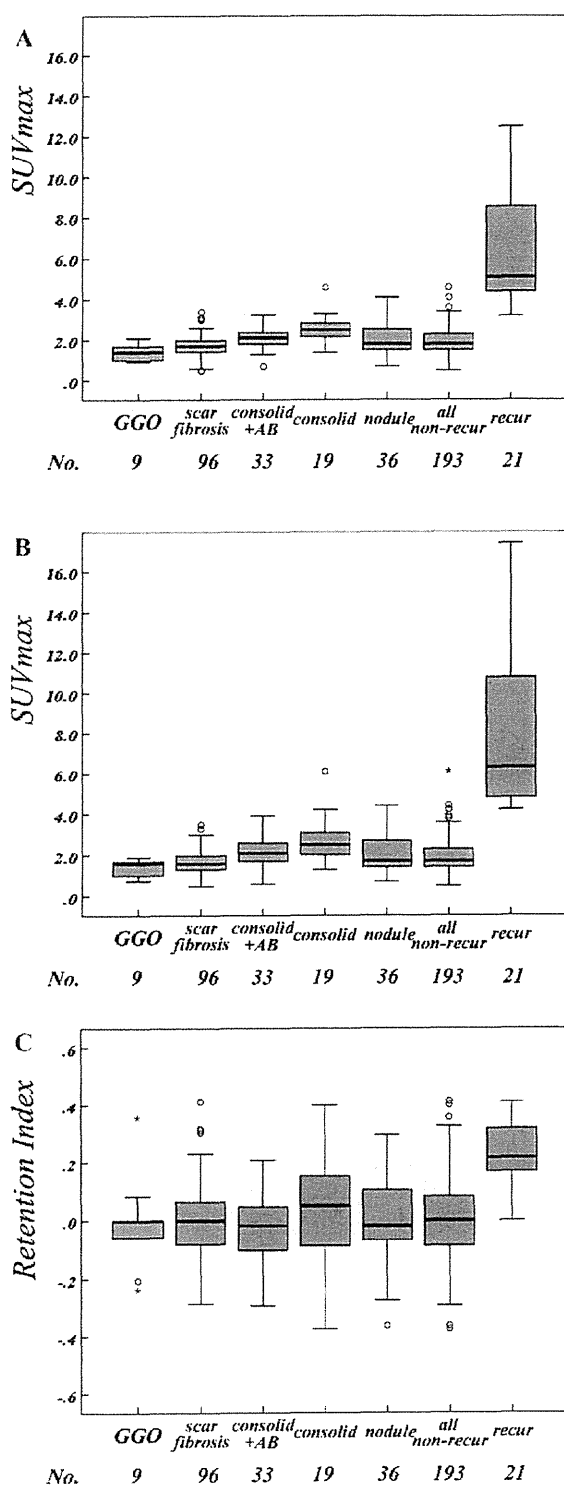
Fig. 4. Box and whisker plot of each factor. Center bold line indicates the median value, and the bottom and top of the box indicate the 25th and 75th percentiles, respectively. Circles indicate outliers. (A) Distribution of maximum standardized uptake values (SUVmaxs) on early images, (B) distribution of SUVmaxs on late images, and (C) distribution of retention indexes.

Currently, ^{18}F-FDG PET/CT is not recommended as a primary surveillance method to detect recurrence or for re-staging patients with stage I or II disease [10]. However, a systematic review suggested that high-risk CT changes with high SUVmaxs (≥5) on ^{18}F-FDG PET might raise suspicion of recurrence from limited

available evidence [11]. This is the first study to systematically evaluate the ability of ^{18}F-FDG PET/CT to differentiate recurrence from RILO for localized NSCLC patients following SBRT.

Radiation lung injuries are divided into radiation pneumonitis and fibrosis. Radiation pneumonitis typically occurs at 1.5–9 months after SBRT [5,12], and often has a graphically dramatic appearance. Radiation fibrosis appears following radiation pneumonitis. The opacity resulting from radiation pneumonitis gradually shrinks and becomes fixed as solid or scar opacity [5,12] and the opacity may exhibit changes in size and shape [3]. However, in our previous report, among 20 patients with such abnormal opacities, only three patients were diagnosed as having recurrence [3]. Therefore, RILO was difficult to differentiate from local recurrence on CT.

In this study, we grouped RILO findings into five categories. Among these categories, three among 22 tumors with consolidation and 17 among 53 tumors with nodule opacity were diagnosed as locally recurrent. These findings suggested that CT had a limited ability to detect local recurrences.

Although ^{18}F-FDG PET/CT is useful for detecting recurrent lesions after conventional radiotherapy for lung cancer [13], the utility of ^{18}F-FDG PET after SBRT is not well established. There are only a few reports that describe ^{18}F-FDG PET findings during a chronic phase after SBRT for lung cancer. SUVmaxs gradually decreased to 2.0–3.1 at later periods in patients with no evidence of local recurrence [3,14,15]. In contrast, Hoopes et al. [16] reported that the SUVs of two patients exceeded 5.0 with no evidence of local recurrence.

This study suggests the utility of ^{18}F-FDG PET for detecting local recurrence based on the optimal threshold SUVmaxs. Optimal thresholds would logically exist in the overlapping zone between the values of the non-recurrence and recurrence. However, the number of recurrences in the overlapping zone was very small ($N = 6$ for early, $N = 9$ for late images). Therefore, the optimal threshold SUVmaxs may change to some extent when more recurrences are observed. Nevertheless, we believe that the usefulness of ^{18}F-FDG PET in the detection of local recurrence would be still validated.

In the evaluation of solitary pulmonary nodules (SPNs), an SUVmax of 2.5 is frequently used as a threshold criterion for malignancy with ^{18}F-FDG PET imaging [17], which was lower than the optimal threshold for local recurrence after SBRT. One reason was that the SUVmax of RILO itself had a slightly higher value; the median SUVmaxs of RILO on early images was 1.8 (range: 0.5–4.6).

In this study the diagnostic accuracies of early and late images for differentiation were nearly equivalent to each other. However, it remains controversial if a diagnosis of malignancy with dual-time-point ^{18}F-FDG PET imaging has a better accuracy than early imaging only; there are contradicting results supporting or rejecting the use of dual-time-point imaging [18,19]. Considering these results and the time spent to acquire a late image and RI, we suggest that acquisition of only an early image followed by calculating the SUVmax would be sufficient to differentiate RILO from recurrence.

This study had several limitations. First, this was a retrospective study. Only 17 tumors on 21 scans were diagnosed as being local recurrence. Secondly, only three tumors could be diagnosed pathologically, while the other patients' diagnoses were based on enlargements on successive CT images. It was often difficult to prove recurrence pathologically. Candidate for SBRT were often elderly and had co-morbidity and, therefore, many of them were treated with no pathological confirmation. In fact, the rate of histologically unproven patients in multinational pooled analysis ($N = 434$) [20], Verstegen et al. ($N = 591$) [21] and our institution ($N = 173$) [22] were 38%, 65% and 33%, respectively. Furthermore, pathological confirmation was more difficult when local recurrence were suspected after SBRT. However, recurrence could be diagnosed on successive CT images, which was often accompanied by